CO_2 reduction on pure Cu produces only H_2 after subsurface O is depleted: Theory and experiment

Guiji Liu[a,b,c,1], Michelle Lee[a,b,d,1], Soonho Kwon[e,f,g,1], Guosong Zeng[b,c], Johanna Eichhorn[a,b,h,i], Aya K. Buckley[a,b,j], F. Dean Toste[a,j], William A. Goddard III[e,f,g,2], and Francesca M. Toma[a,b,c,2]

[a]Joint Center for Artificial Photosynthesis, Lawrence Berkeley National Laboratory, Berkeley, CA 94720; [b]Chemical Sciences Division, Lawrence Berkeley National Laboratory, Berkeley, CA 94720; [c]Liquid Sunlight Alliance, Lawrence Berkeley National Laboratory, Berkeley, CA 94720; [d]Department of Chemistry and Chemical Biology, Cornell University, Ithaca, NY 14853; [e]Materials and Process Simulation Center, California Institute of Technology, Pasadena, CA 91125; [f]Joint Center for Artificial Photosynthesis, California Institute of Technology, Pasadena, CA 91125; [g]Liquid Sunlight Alliance, California Institute of Technology, Pasadena, CA 91125; [h]Walter Schottky Institut, Technische Universität München, 85748 Garching, Germany; [i]Physik Department, Technische Universität München, 85748 Garching, Germany; and [j]Department of Chemistry, University of California, Berkeley, CA 94720

Edited by Michael L. Klein, Temple University, Philadelphia, PA, and approved April 13, 2021 (received for review June 18, 2020)

We elucidate the role of subsurface oxygen on the production of C_2 products from CO_2 reduction over Cu electrocatalysts using the newly developed grand canonical potential kinetics density functional theory method, which predicts that the rate of C_2 production on pure Cu with no O is ∼500 times slower than H_2 evolution. In contrast, starting with Cu_2O, the rate of C_2 production is >5,000 times faster than pure Cu(111) and comparable to H_2 production. To validate these predictions experimentally, we combined time-dependent product detection with multiple characterization techniques to show that ethylene production decreases substantially with time and that a sufficiently prolonged reaction time (up to 20 h) leads only to H_2 evolution with ethylene production ∼1,000 times slower, in agreement with theory. This result shows that maintaining substantial subsurface oxygen is essential for long-term C_2 production with Cu catalysts.

electrocatalysis | hydrogen evolution reaction | ethylene evolution | grand canonical potential kinetics | DFT

Anthropogenic carbon emissions, particularly CO_2, are surging primarily because of global fossil fuel consumption, raising serious environmental concerns about global warming (1). Recycling CO_2 via electrochemical (EC) reduction of carbon dioxide (CO_2RR) to fuels and valuable chemicals using renewable energy could play an important role in global efforts to address current energy demand and climate challenges (2). CO_2 can be electrochemically reduced to C_1 products (CO, methane, and formic acid), C_2 products (ethylene, ethane, and ethanol), and C_3 products (*n*-propanol) (3, 4). The major challenge to make this process economically viable is to increase selectivity to generate higher-hydrocarbon products.

In this context, copper (Cu) remains the only single metal capable of producing significant amounts of higher hydrocarbons, such as C_2 products ethylene or ethanol. Indeed, many experiments report that oxide-derived Cu catalysts lead to higher activity for C_2 products (5–8). However, the role of oxygen in the Cu catalyst and the correlation with the underlying C_2 production mechanism remains a subject of considerable debate (4). We suggested earlier that the optimum catalyst is the partially reduced cuprous oxide (Cu_2O) surface in which surface and/or subsurface oxygen of Cu_2O are adjacent to a reduced Cu^0 surface, termed MEOM for metal embedded in oxidized matrix (9). Density functional theory (DFT) calculations on model systems showed that MEOM leads to a barrier for CO_2 reduction to CO that is 0.22 eV lower than for pure Cu^0 and to a barrier for CO dimerization (the first step toward C_2 products) that is 0.39 eV lower than for pure Cu^0. This result suggests that C_2 production on the MEOM surface could be >5,000 times faster than for pure Cu^0. Indeed, other groups have recently hypothesized that surface Cu^+ and/or subsurface oxygen on Cu might play an essential role in promoting CO dimerization and ethylene production (10–14). However, others have argued that such surface or subsurface oxygen species cannot be important because many experiments show that surface oxygen is rapidly depleted under CO_2RR conditions (15, 16), and it is, rather, suggested that surface roughness plays an active role in bolstering ethylene selectivity (16, 17). Hence, fundamental understanding into the relationship between the presence of oxygen and the increased C_2 production activity on Cu catalyst can solve the existing debates.

Here, we combine theory and experiments to disentangle the contributions from both Cu that contains oxygen and fully reduced (or depleted) Cu^0 to uncover the role of subsurface oxygen in promoting C–C coupling and consequently C_2 production on Cu catalysts. We predict that hydrogen evolution reaction (HER) on pure Cu(111) leads to a turnover frequency (TOF) = 0.32/s, in stark contrast to C_2 production, which we predict to have a TOF = 0.0006/s, which is ∼500 times slower than HER. Our time course experiments confirm these predictions, showing that, when continuing CO_2 reduction for times up to 20 h, the C_2 production rates decrease to a level of 1,600 and 680 times slower than HER on polycrystalline Cu and Cu_2O catalysts, respectively.

In contrast, starting with Cu_2O, we find that the reduction leads to a Cu^0/Cu_2O structure, with a thin, disordered Cu^0 surface on top of the Cu_2O substrate. We calculate that this structure leads to TOF = 3.95/s for C_2 production compared to TOF = 10.02/s for HER, which is 2.58 times faster. This result is consistent with our experiments, which find HER production to be 2.1 times higher than C_2 during the first 5 h. In addition, we predict that C_2 production on the Cu^0/Cu_2O model is a factor of 5,000 times faster

Significance

Electrochemical reduction of CO_2 to fuels and valuable chemicals is a global imperative to address energy and climate challenges. Despite enormous efforts, there is not yet a commercial process. The best catalyst remains Cu metal, but a great deal of controversy revolves around the role of the presence of oxygen in the material. We combine theory and experiments to show that pure Cu without subsurface oxygen leads to no organic products. Thus, maintaining substantial oxygen at Cu surfaces is essential for long-term reduction of CO_2 to organics.

Author contributions: G.L., M.L., S.K., F.D.T., W.A.G., and F.M.T. designed research; G.L., M.L., S.K., and G.Z. performed research; J.E. and A.K.B. performed preliminary measurements; G.L., M.L., S.K., W.A.G., and F.M.T. analyzed the data; and G.L., M.L., S.K., F.D.T., W.A.G., and F.M.T. wrote the paper.

The authors declare no competing interest.

This article is a PNAS Direct Submission.

[1]G.L., M.L., and S.K. contributed equally to this work.

[2]To whom correspondence may be addressed. Email: wagoddard3@gmail.com or fmtoma@lbl.gov.

This article contains supporting information online at https://www.pnas.org/lookup/suppl/doi:10.1073/pnas.2012649118/-/DCSupplemental.

Published June 3, 2021.

than that on pure Cu(111). Indeed, our experiments measured an initial partial current density of ethylene production on Cu_2O of 0.6 to ~0.8 mA/cm^2, which becomes negligible after 20 h on fully depleted Cu (~1/1,000 of the H_2 current).

These calculations of TOF as a function of applied potential (U) use our recently developed grand canonical potential kinetics (GCP-K) methodology that predicts the evolution of the reaction intermediates and transition states (TSs) in solvent to obtain the TOF as a function of U (18). In this approach, the solvated structures and energetics of the intermediates adjust adiabatically as the U is changed, leading to very accurate rates versus U. Here, we apply GCP-K to directly assess the impact of subsurface oxygen on the C_2 production over Cu catalysts. Many theoretical studies have been reported on the product distribution during CO_2RR, but nearly all were carried out for fixed charge, usually zero. None have previously considered optimizing structure and kinetic activation energies as a function of U (19–23). In this study, we consider all thermodynamically stable structures of Cu_2O using GCP-K DFT calculations at U = −1 V_{RHE} with pH 7, common experimental conditions for examining the activity of Cu-based catalysts in CO_2RR (6, 17). Here, the U is U = −1 V on the reversible hydrogen electrode (RHE) scale. The GCP-K formulation allows the geometries to relax as U is changed so that the microkinetics allows all structures (equilibrium states and saddle points for TSs) to remain optimum for each U. This development enables us to track the free energy continuously with U at a computational cost close to conventional canonical DFT calculations (see *SI Appendix* for further details of GCP-K method, *SI Appendix*, Figs. S1 and S2).

First, we performed GCP-K calculations to construct the surface Pourbaix diagram shown in Fig. 1*A*. Starting from intact Cu_2O(111), we gradually reduced the surface by removing various numbers of oxygen and plotted the free energies of eight states (*SI Appendix*, Fig. S3 and Table S1), as a function of U. The results show that the disordered Cu^0/Cu_2O surface is more stable at −1 V_{RHE} than the MEOM and Cu_2O models. Therefore, we considered the Cu^0/Cu_2O model as the structure for Cu_2O at −1 V_{RHE}. We assume for the pure Cu with no O that the catalyst relaxes back to Cu(111) (*SI Appendix*, Fig. S4), using this as the model for fully depleted Cu_2O or Cu. We consider the MEOM surface for comparison in

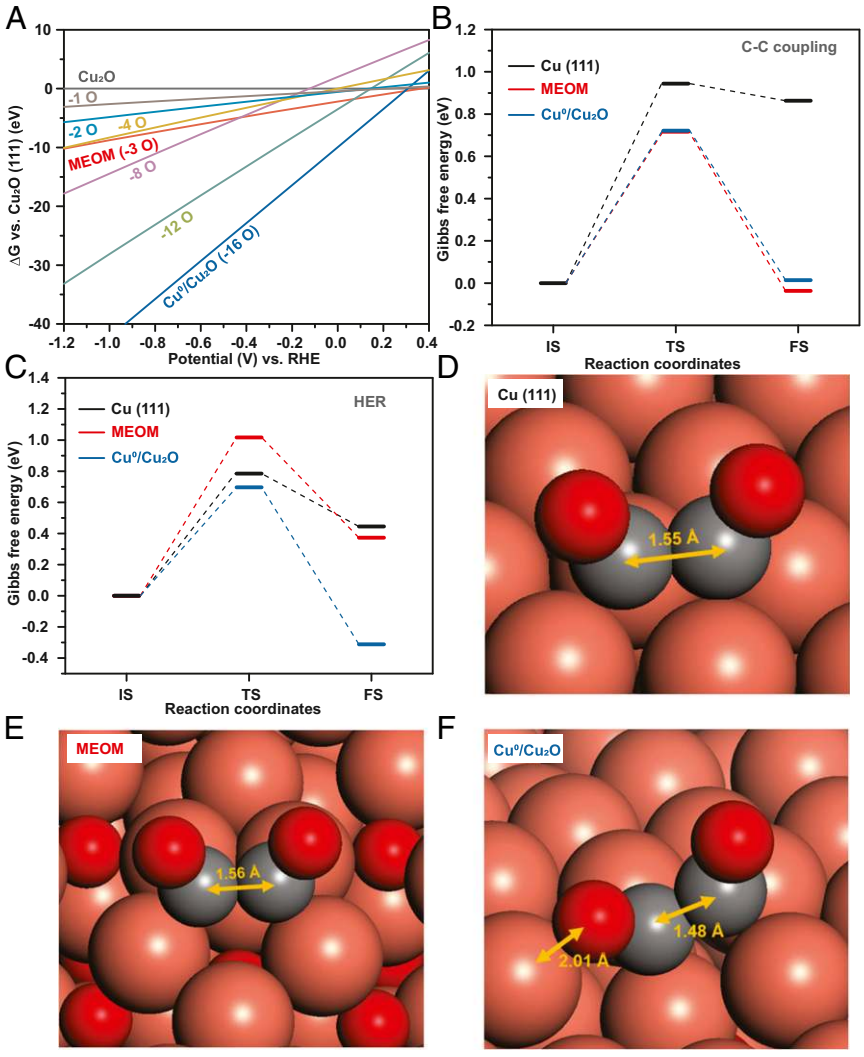

Fig. 1. GPC-K DFT calculations for different Cu phases and their relation to C_2 production. Surface free energies as a function of U of various surface phases with different numbers of reduced lattice oxygen potential energy surfaces for the CO dimerization (*A*), the RDS for C_2 production (*B*), and the RDS for HER at U = −1 V_{RHE} and pH 7 on Cu(111), MEOM, and Cu^0/Cu_2O (*C*). The RDS are the Heyrovsky step [H_{ad}+H_2O(l) + e^- → H_2(g) +OH^-(aq)] for Cu(111) and MEOM and the Volmer step [H_2O(l) + e^- → H_{ad}+ OH^-(aq)] for Cu^0/Cu_2O. OCCO* geometries on Cu(111) (*D*), OCCO* geometries on MEOM (*E*), and OCCO* geometries on Cu^0/Cu_2O catalysts (*F*). The Us for each state correspond to −1.25 V_{RHE}, −1.15 V_{RHE}, and −1.02 V_{RHE}, respectively. The C–C bond distances are indicated for all catalysts, and Cu–O bond distance is also indicated for Cu^0/Cu_2O catalysts.

SI Appendix. We predicted the free energy barriers for HER and for CO dimerization (the dominant step in C_2 formation) for these models.

Our previous full solvent quantum mechanics molecular dynamics studies showed that C–C coupling of two surface CO is the rate determining step (RDS) for producing C_2 products (24). We predict that the $\Delta G\dagger = 0.72$ eV for C–C coupling on the disordered Cu^0/Cu_2O surface (Fig. 1*B*) led to TOF = 3.95/s, which is 5,840 times faster than our predicted to 6.77×10^{-4}/s for oxygen depleted Cu(111) surface, which has a barrier of $\Delta G\dagger$ = 0.94 eV [close to our previous results (9)]. This enhancement of C–C coupling on Cu^0/Cu_2O is attributed to its capability of forming a (OCC)O–Cu bond, which greatly stabilizes OCCO*, as shown in Fig. 1*F* and *SI Appendix*, Fig. S3.

For HER, we considered the following:

- Volmer [$H_2O(l) + e^- \rightarrow H_{ad}$+$OH^-(aq)$] step and
- Heyrovsky [H_{ad}+$H_2O(l) + e^- \rightarrow H_2(g)$ +$OH^-(aq)$] step.

Fig. 1*C* examines both steps on Cu(111) as a function of U.

On Cu(111) at U = −1 V_{RHE}, the RDS for the HER is Heyrovsky, which leads to $\Delta G\dagger = 0.79$ eV (0.16 eV lower than for C–C coupling) and to TOF = 0.32/s.

For Cu^0/Cu_2O at U = −1 V_{RHE}, we find the RDS for the HER to be the Volmer reaction with $\Delta G\dagger = 0.70$ eV, only −0.02 eV lower than C–C coupling.

Thus, the C_2 production rate is predicted to be comparable to HER rate on Cu^0/Cu_2O (0.39 times slower). Whereas on fully depleted Cu(111), the predicted rate for H_2 production is 479 times higher than C_2 production. The predicted ratio of the rate for H_2 production on Cu^0/Cu_2O versus fully depleted Cu(111) is 3.14×10^1. All atomic configurations for catalytic reactions are shown in *SI Appendix*, Figs. S6–S8.

To validate experimentally the above predictions from theory, we synthesized Cu-based catalysts through EC deposition of Cu_2O on polycrystalline Cu. Compared to the planar surface of polycrystalline

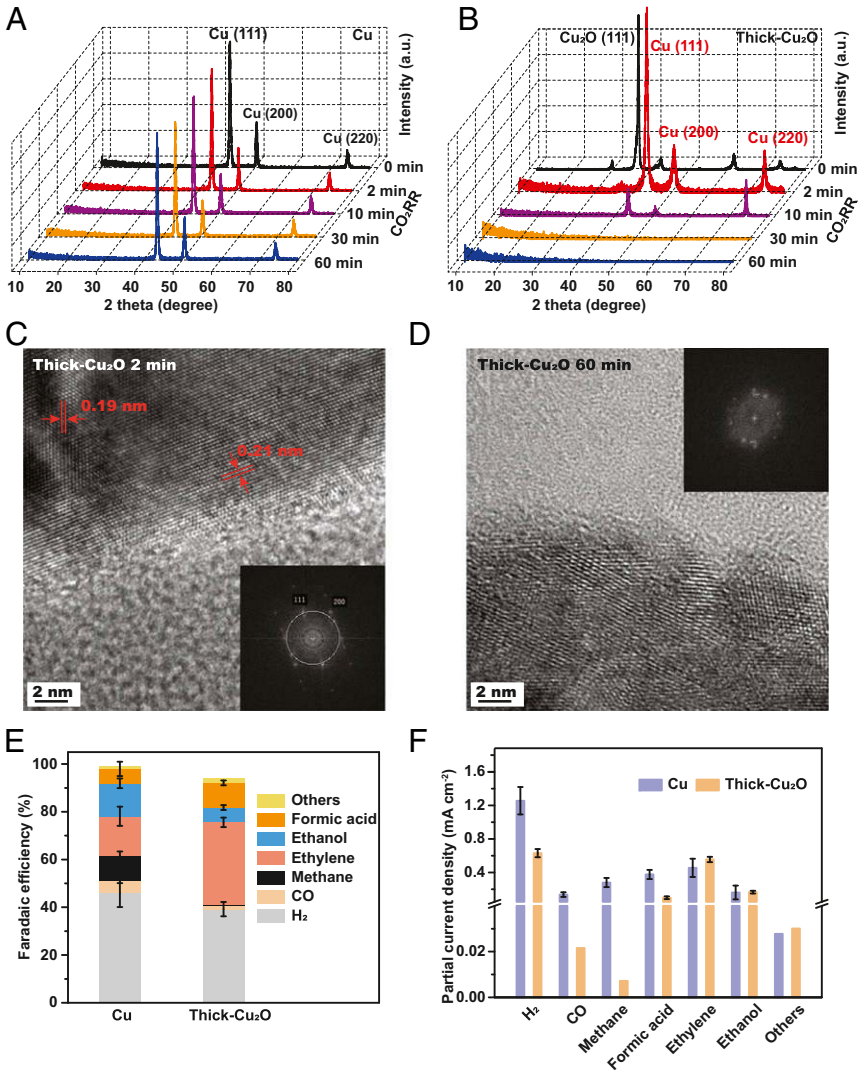

Fig. 2. Stable phases and catalytic activities of polycrystalline Cu and thick Cu_2O under CO_2RR. Ex situ GIXRD analysis of polycrystalline Cu (*A*) and thick Cu_2O (*B*) after 0 (as-prepared), 2, 10, 30, and 60 min CO_2RR at −1 V_{RHE} in 0.1 M CO_2-saturated K_2CO_3 electrolyte (pH 7). High-resolution transmission electron microscopy images of thick Cu_2O under CO_2RR for 2 min (*C*) with corresponding fast Fourier transform (*Inset*) and 1 h (*D*) with corresponding fast Fourier transform (*Inset*); fragmented Cu-based nanoparticles with lower crystallinity were observed over 1 h CO_2RR. (*E*) FEs of CO_2RR toward H_2 (gray), CO (gold), methane (black), ethylene (pink), ethanol (blue), formic acid (orange), and others: acetate, ethylene glycol, and 1-propanol (yellow) for Cu and thick Cu_2O at −1 V_{RHE}. (*F*) Partial current densities toward H_2, CO, methane, formic acid, ethylene, ethanol, and others: allyl alcohol; *n*-propanol, normalized by electrochemically active surface area over Cu (purple); and thick Cu_2O (orange) for 1 h CO_2RR at −1 V_{RHE} in CO_2-saturated 0.1 M K_2CO_3 electrolyte (pH 7). Average values in *E* and *F* are based on triplicates, and the errors correspond to the SEM of data points from individual samples in *SI Appendix*, Table S3.

Cu, our synthesized Cu_2O samples exhibit polycrystalline grains with a 1-μm thickness (*SI Appendix*, Fig. S9), which we refer to as thick Cu_2O.

Under bulk electrolysis at −1 V_{RHE} with CO_2-saturated 0.1 M K_2CO_3 electrolyte for 65 min, the crystalline structures of polycrystalline Cu featuring Cu(111) are retained, as shown in ex situ grazing incidence X-ray diffraction (GIXRD) analysis (Fig. 2*A*)

On the other hand, thick Cu_2O is reduced to Cu^0 because of removal of lattice oxygen under CO_2RR, leading to disordered Cu^0 surface over time, as demonstrated by ex situ GIXRD (Fig. 2*B*). Complementary high-resolution transmission electron microscopy confirms that the surface of thick Cu_2O is readily reduced to crystalline Cu^0 after 2 min of CO_2RR (Fig. 2*C*). Then, this crystalline surface evolves into fragmented and disordered Cu-based nanoparticles over 60 min CO_2RR (Fig. 2*D*), in excellent agreement with GIXRD results. Control experiments further revealed that thick Cu_2O became crystalline Cu^0 under N_2 saturation at −1 V_{RHE} and at less negative potentials (−0.6 V_{RHE} and −0.3 V_{RHE}) under CO_2RR for 1 h (*SI Appendix*, Fig. S10). Thus, these experimental observations verify that the theoretically predicted Cu(111) and disordered Cu^0/Cu_2O model are indeed the thermodynamically stable structure for polycrystalline Cu and thick Cu_2O under CO_2RR at −1 V_{RHE}.

The initial catalytic activity and selectivity of polycrystalline Cu and thick Cu_2O catalysts toward CO_2RR were examined over 1 h by gas chromatography and high-performance liquid chromatography in a two-compartment flow cell (*SI Appendix*, Fig. S11). Compared to polycrystalline Cu, we find that using thick Cu_2O catalysts leads to lower selectivity of H_2 evolution, while selectivity toward C_2 (ethylene and ethanol) products over C_1 (CO, methane, and formic acid) products is higher (Fig. 2*E*), in agreement with previous reports (25, 26). In particular, the C_2/C_1 ratio reaches a value of 5.9 on thick Cu_2O, while that for polycrystalline Cu is only 0.8, based on the faradaic efficiencies (FEs) in Fig. 2*E*. In addition to FE, to understand the intrinsic activity toward each product, we further plotted partial current density, normalized by electrochemically active surface area, for polycrystalline Cu and thick Cu_2O catalysts in Fig. 2*F*. These data highlight that the enhanced C_2/C_1 ratio on thick Cu_2O mainly stems from suppression of C_1 products, while similar rates of C_2 (ethylene and ethanol) products were observed on polycrystalline Cu and thick Cu_2O catalysts during the first hour of measurements. Previous studies have shown that the activity and selectivity of C_2 production on Cu are strongly dependent on the surface morphology and chemical composition (14, 17, 27).

To assess the role of surface morphology on Cu and thick Cu_2O catalysts under operating conditions, we employed quasi–in situ EC atomic force microscopy (Fig. 3). Compared to as-prepared polycrystalline Cu (0 min), no dramatic topography change was observed on Cu under CO_2RR with a constant R_a (~2 nm) (Fig. 3 *A*–*C*). On the other hand, EC fragmentation occurred on the thick Cu_2O catalysts along with nanoparticles formation on Cu_2O grains during the first 1 min of EC measurements (Fig. 3 *D* and *E*). Afterward, the changes in topography remain small on thick Cu_2O (Fig. 3 *E* and *F*), leading to constant R_a (~21 nm), which is 10 times of that of polycrystalline Cu. The sharp discrepancy in surface topography and roughness of polycrystalline Cu and thick Cu_2O rules out the possibility that surface topography or roughness play a predominant role in the similar C_2 production rate on polycrystalline Cu and thick Cu_2O.

As a result, we argue that a similar initial chemical composition in polycrystalline Cu and thick Cu_2O is key to achieve the similar activity of ethylene production, as supported by the results during the first hour of activity of Cu and thick Cu_2O samples (Fig. 2). Specifically, X-ray photoelectron spectroscopy (XPS) reveals that polycrystalline Cu initially possesses native oxide surface layers (*SI Appendix*, Fig. S12), as it is well known that Cu is readily oxidized in air (16). The coexistence of native surface oxygen and Cu^0 substrate makes the polycrystalline Cu surface similar to a very thin MEOM structure. Meanwhile, the disordered Cu^0 character was naturally formed on thick Cu_2O under CO_2RR, as shown in Fig. 2 *B*–*D*. Thus, similar rates for C_2 products obtained on polycrystalline Cu and Cu_2O during 1 h CO_2RR can be interpreted by taking into account that MEOM structure of polycrystalline Cu and the disordered Cu^0 character of thick Cu_2O share a similar kinetic barrier for C–C coupling, as mentioned earlier. However, as native oxygen on polycrystalline Cu is depleted under CO_2RR at −1 V_{RHE}, the population of the thin MEOM structure will decrease rapidly over time. In addition, theoretical calculations suggest that disordered Cu^0 surface in thick Cu_2O would ultimately

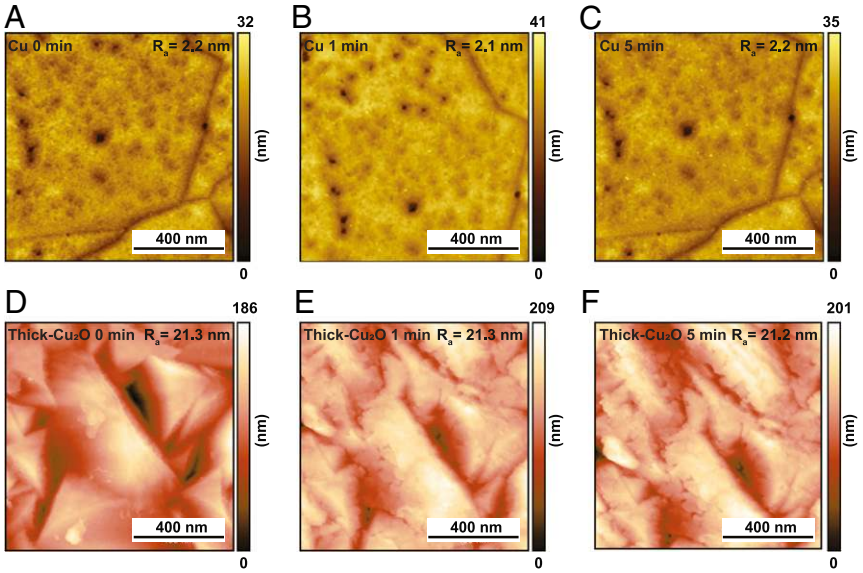

Fig. 3. Monitoring surface topography or roughness over Cu and thick Cu_2O under CO_2RR. Quasi–in situ EC-AFM images of polycrystalline Cu at 0 min (as-prepared) (*A*), 1 min (*B*), and 5 min (*C*) and thick Cu_2O at 0 min (as-prepared) (*D*), 1 min (*E*), and 5 min (*F*) in 0.1 M CO_2-saturated K_2CO_3 electrolyte (pH 7) at −0.8 V_{RHE}.

stabilize to crystalline Cu^0 after oxygen is fully depleted. In this context, we consider that the long-term CO_2RR selectivity and activity toward ethylene on polycrystalline Cu and Cu_2O catalysts should be time dependent, which is associated with oxygen depletion. As residual oxygen is removed completely and disordered, Cu^0 transforms to pure crystalline Cu^0, leading to H_2 as the dominant product, in excellent agreement with the predictions by the DFT calculations.

To validate this hypothesis, we further synthesized a thin Cu_2O with 0.2-μm thickness (*SI Appendix*, Fig. S13) to compare with the results for thick Cu_2O. We proceeded to carry out long-term measurements (15 to 25 h) of product distributions on polycrystalline Cu, thin Cu_2O, and thick Cu_2O at −1 V_{RHE} with CO_2-saturated 0.1 M K_2CO_3 electrolyte. We monitored hourly gaseous ethylene and H_2 producing rates over time (Fig. 4), as well as the corresponding full products detection over the measured time (*SI Appendix*, Figs. S14 and S15). The total FEs are close to 100% for all samples.

As expected, selectivity and production rate of ethylene rapidly decayed on polycrystalline Cu catalyst within 1 h because of the depletion of native oxygen, while the HER rates increase with time. Furthermore, we employed a suit of characterizations including cyclic voltammetry, inductively coupled plasma mass spectrometry, and XPS analysis to exclude the role of surface texturing and metal ion contamination in determining the selectivity switch from ethylene to H_2 on polycrystalline Cu (*SI Appendix*, Figs. S16 and S17 and Table S4).

By contrast, the selectivity and production rate of ethylene on thin Cu_2O and thick Cu_2O slightly increased over the first 4 h, followed by a slow decay over time. Ultimately, C_2 production goes eventually to a level 1,600 times smaller than HER for polycrystalline Cu and 680 times lower for Cu_2O catalysts, in excellent agreement with theory predictions. In particular, for all cases, ethylene production finally became negligible with sufficient time: ∼4 h for polycrystalline Cu, ∼15 h for thin Cu_2O, and ∼20 h for thick Cu_2O.

Moreover, we demonstrated that after 16 h CO_2RR, polycrystalline Cu, thin Cu_2O, and thick Cu_2O catalysts were all able to recover their initial selectivity toward ethylene production: 92, 77, and 78% of their initial activity, respectively (Fig. 4*G*). This result was obtained by simply allowing the samples to regain a native oxide layer via reoxidization in the air.

Taking these results together, we conclude that the activity and selectivity of polycrystalline Cu and Cu_2O catalysts toward ethylene are influenced dramatically by the oxygen content within the Cu-based catalysts.

This interpretation was further corroborated by angle-resolved XPS (AR-XPS) analysis over as-prepared polycrystalline Cu, Cu after 1 h CO_2RR, and Cu after 16 h CO_2RR (*SI Appendix*, Figs. S18–S20). To minimize the oxidation of the sample in air, the sample was rinsed, dried with N_2 flow, and transferred to the vacuum chamber of XPS within 2 min after the CO_2RR measurements were completed. The O 1-s spectra show that lattice oxygen decreases with increasing takeoff angle on both as-prepared polycrystalline Cu and Cu after 1 h CO_2RR, indicating that subsurface lattice oxygen is present (28). In contrast, only surface-adsorbed OH/H_2O is observed on polycrystalline Cu after 16 h CO_2RR (*SI Appendix*, Fig. S18 and Table S5), which is consistent with Cu 2p and Cu Auger transition (Cu $L_3M_{4,5}M_{4,5}$, *SI Appendix*, Figs. S19 and S20).

It is important to note that in situ Raman measurements at −1 V_{RHE} indicate that the total reduction of thick Cu_2O was most likely completed in 1 h (*SI Appendix*, Fig. S21), which is shorter than the critical time for the selectivity switch from ethylene to H_2, observed in Fig. 4. By contrast, we find that the time scale of the relaxation of disordered Cu^0 into crystalline Cu^0 is much longer than that one of Cu_2O reduction, which agrees well with the time scale of the switch in selectivity (*SI Appendix*, Fig. S22). Thus, we propose that the lagging change on C_2 production, compared with Cu_2O reduction, is most likely due to the slow relaxation of disordered Cu^0 into crystalline Cu^0. While Raman spectroscopy measurements exclude the presence of an underlayer of (partially reduced) Cu_2O after 1 h, previous studies showed that disordered Cu^0 can have more labile oxygen in the lattice during CO_2RR (6, 12). Moreover, Cuenya et al. suggested that the K^+ cation in the electrolyte may be able to retain the removal of subsurface oxygen species under CO_2RR (29).

In addition, our theoretical calculations (*SI Appendix*, Fig. S4) find that the disordered Cu^0 relaxes back to Cu(111) after oxygen is fully depleted. While the relationship between slow crystalline relaxation and residue oxygen requires further investigations, the comparison of AR-XPS analysis over as-prepared thick Cu_2O, thick Cu_2O after 1 h, and after 16 h CO_2RR (*SI Appendix*, Fig. S23 and Table S6) reveals that subsurface oxygen is observed on thick Cu_2O after 1 h CO_2RR but is absent after 16 h CO_2RR. This result implies that residual oxygen is retained in the lattice, even after Cu_2O was reduced.

These findings highlight the essential role of subsurface oxygen in C_2 production on Cu-based catalysts and how this role is related to inducing the formation of disordered Cu^0. The disordered Cu^0 structure represents the thermodynamically stable structure of Cu_2O-based catalysts under CO_2RR, which substantially enhances intrinsic C_2 production, compared to pure crystalline Cu^0. This phase is achieved by dynamic transformation of Cu-based nanocrystals under CO_2RR conditions (6, 30).

While previous studies on subsurface oxygen on Cu demonstrate that subsurface oxygen may not play an essential role in CO_2 adsorption (31), Nilsson and coworkers show that subsurface oxygen on Cu is instrumental in enhancing CO adsorption, which can lead to an improved C_2 selectivity (32, 33).

We calculate C_2 and HER TOFs on various Cu-based models. These results demonstrate that the presence of residual oxygen is essential for retention and long-term stability of the disordered Cu^0 surface that is active toward C_2 production. This finding can explain why disordered Cu-based catalysts and uncoordinated Cu sites at grain boundaries have higher selectivity for C_2 products (6, 8, 34). Thus, allowing the residual oxygen of Cu catalysts to be replenished from other robust oxides under CO_2RR might be a promising direction to design efficient CO_2RR catalysts with sustained C_2 selectivity. Additionally, the intrinsic ability of Cu to be rapidly oxidized in the air to regain its catalytic ability is beneficial to developing a sustainable/recyclable catalyst. For example, recent findings show that the continuous regeneration of defects and Cu^+ species favors C–C coupling pathways (14).

In summary, we provide mechanistic insights into C_2 production over Cu-based catalysts by GCP-K DFT calculations, showing that for pure Cu(111) with no subsurface oxygen, the rate of C_2 production is ∼500 times smaller than HER, whereas reduced models starting with Cu_2O led to C_2 production ∼10,000 times faster. Furthermore, we combine time-dependent product detection with a correlative characterization approach to confirm that activity and selectivity of polycrystalline Cu and Cu_2O catalysts toward ethylene is determined by the disordered Cu^0 character involving oxygen content within Cu-based catalysts. Compared to the MEOM structure, the formation of a disordered Cu^0 surface induced by the removal of lattice oxygen from Cu_2O is thermodynamically favorable under CO_2RR. After long-term CO_2RR, pure crystalline Cu^0 without subsurface oxygen leads only to HER at −1 V_{RHE} in aqueous solutions, in excellent agreement with the DFT calculations. Based on this theoretical and experimental understanding, we conclude that the key for the rational development of highly active electrocatalysts toward C_2 production is to modify the catalyst conditions in such a way as to preserve surface or subsurface oxygen in the Cu catalyst under CO_2RR conditions.

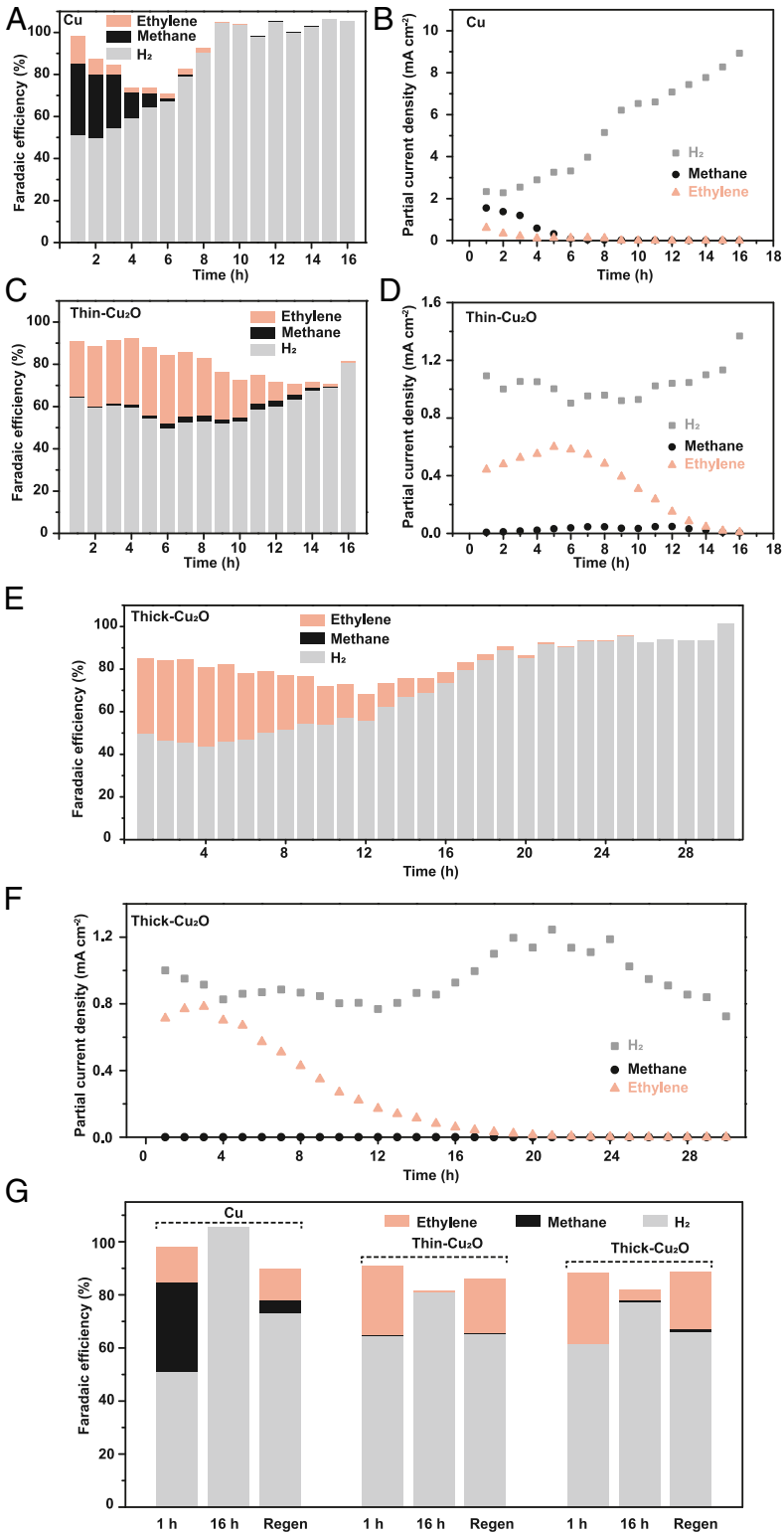

Fig. 4. Long-term CO_2RR measurements on polycrystalline Cu, thin Cu_2O, and thick Cu_2O. (*A*) FE of polycrystalline Cu; (*B*) partial current densities of polycrystalline Cu toward H_2, methane, and ethylene, normalized by electrochemically active surface area (ECSA); (*C*) FE of thin Cu_2O; (*D*) partial current densities of thin Cu_2O, toward H_2, methane, and ethylene, normalized by ECSA; (*E*) FE of thick Cu_2O; (*F*) partial current densities of thick Cu_2O, toward H_2, methane, and ethylene, normalized by ECSA at -1.0 V_{RHE} in CO_2-saturated 0.1 M K_2CO_3 electrolyte (pH 7) for CO_2RR over time. (*G*) FE of Cu, thin Cu_2O, and thick Cu_2O at -1.0 V_{RHE} in CO_2-saturated 0.1 M K_2CO_3 electrolyte (pH 7) after 1 h CO_2RR, 16 h CO_2RR, and Cu, thin Cu_2O and thick Cu_2O experienced 16 h CO_2RR, followed by a regeneration process: allowing the above catalysts to sit in air for about 2 wk.

Materials and Methods

Electrodeposition of Cu_2O. In a typical experiment, a 0.4 M Cu sulfate pentahydrate solution was used as the plating solution, prepared by stirring 4.99 g $CuSO_4{\cdot}5\ H_2O$ in 50 mL MilliQ water. A total of 3 M (13.51 g) lactic acid was added to stabilize Cu^{2+} in basic solution, and then, 3 M NaOH was added to the solution until the pH of plating solution reached 12. Thick Cu_2O and thin Cu_2O were deposited on Cu foils (99.999%, Alfa Aesar) for 150 and 15 min, respectively, at a constant current density (−0.1 mA/cm^2) in a three-electrode configuration under room temperature. To obtain a uniform coating, the Cu foil was mechanically polished with sandpapers (1,200 g Wetordry sandpaper, 3 M) and electropolished in 85% phosphoric acid at +2.1 V for 5 min, followed by annealing in air at 300 °C for 30 min prior to use. After the deposition, the sample was gently rinsed with MilliQ water and then dried with a nitrogen gun.

Product Detection. EC experiments were conducted in a two-compartment flow cell fabricated from polyether ether ketone. A Selemion anion-exchange membrane separated the two chambers. A Pt foil was used as the counter electrode. A leak-free Ag/AgCl electrode (LF-1, 1-mm outer diameter, Innovative Instruments, Inc.) was used as the reference electrode.

Computational Details. Our DFT calculations used the Vienna ab initio simulation package (VASP) (35, 36) with the VASPsol solvation model (37) for geometry optimization, followed by single-point calculations using the charge-asymmetric nonlocally determined local-electric solvation model (CANDLE) (38), as incorporated in the joint density-functional theory (JDFTx) (39).

The electron exchange and correlation were treated within the generalized gradient approximation (40) in the form of the Perdew–Burke–Ernzerhof functional, including the D3 correction for London Dispersion (van der Waals attraction) (41). The interaction between the ionic core and the valence electrons was described by the projector-augmented wave method (42). We used a plane-wave basis up to an energy cutoff of 500 eV. The Brillouin zone was sampled using the $3 \times 3 \times 1$ Monkhorst–Pack grid (43). The convergence criteria for the electronic structure and the atomic geometry were 10^{-5} eV and 0.03 eV/Å for initial state (IS) and final state (FS) and 0.01 eV/Å for TS, respectively. We exploited the variational transition state (TS) theory package to search the TS using both climbing-image nudged elastic band method (44) and the dimer method for TS search (45).

The Gibbs free energies were calculated at 298 K and 1 atm as the following:

$$G = H - T\Delta S = E_{DFT} + E_{ZPE} + E_{solv} + \int_0^{298} C_v dT - T\Delta S,$$

where E_{DFT} is the total energy, E_{ZPE} is zero-point vibrational energy, E_{solv} is the solvation energy, $\int_0^{298} C_v dT$ is the enthalpy, and ΔS is the change in entropy. The turnover frequency (TOF) of a reaction is given by

$$\mathrm{TOF} = \frac{k_B T}{h}\, exp\left(\frac{\Delta G^{\ddagger}}{k_B T}\right)[/s],$$

where k_B is the Boltzmann constant, T is the room temperature (298 K), h is the Plank's constant, and $\Delta G^{\ddagger}$ is a free energy barrier.

The Cu(111) system was described by four layers of 4×4 supercell with two bottom layers fixed. Pristine Cu_2O and oxide-derived Cu were described by four trilayers of 4×4 supercell with two bottom trilayers fixed. The model system was described by three layers of 4×4 Cu slab with 20 Å of vacuum. The bottom two layers are fixed. All designed models have > 20 Å vacuum.

H_2 and C_2 Production on Cu MEOM Model. In a previous study, we suggested that the MEOM model's surface has adjacent-oxidized and metallic regions (9). On MEOM, we predict that C–C coupling has a kinetic barrier of 0.71 eV, which is 0.4 eV lower compared to that on Cu(111). We showed that the enhancement of C–C coupling on this catalyst is due to the attractive electrostatics, involving a carbon on the positively charge Cu^+ induced by subsurface oxygen next to a C bound to a Cu^0 site.

In our calculation on this MEOM catalyst using the GCP-K method, we find that C–C coupling has a kinetic barrier of $\Delta G^{\dagger} = 0.72$ eV, while the RDS for HER (the Heyrovsky reaction) has a barrier of $\Delta G^{\dagger} = 1.02$ eV. This leads to a C_2/H_2 ratio of 1.23×10^6. Compared to Cu(111), C–C coupling is 7.03×10^3 times faster, but HER is 1.19×10^{-4} times slower.

All configurations for IS, TS, and FS of C–C coupling and Volmer and Heyrovsky reactions are depicted in *SI Appendix*, Figs. S6–S8.

Data Availability. All study data are included in the article and/or *SI Appendix*.

ACKNOWLEDGMENTS. This study is based on work initiated with funding from the Joint Center for Artificial Photosynthesis, a Department of Energy (DOE) Energy Innovation Hub, supported through the Office of Science of the US DOE under Award DE-SC0004993 and completed with funding from the Liquid Sunlight Alliance (LiSA), which is supported by the US DOE, Office of Science, Office of Basic Energy Sciences, Fuels from Sunlight Hub under Award DE-SC0021266. Raman spectroscopy and some of the theoretical calculations were specifically supported by LiSA. Work at the Molecular Foundry was supported by the Office of Science, Office of Basic Energy Sciences, of the US DOE under Contract No. DE-AC02-05CH11231. These studies used the Extreme Science and Engineering Discovery Environment which is supported by National Science Foundation Grant ACI-1548562.

1. C. F. Shih, T. Zhang, J. Li, C. Bai, Powering the future with liquid sunshine. *Joule* **2**, 1925–1949 (2018).
2. P. De Luna *et al*., What would it take for renewably powered electrosynthesis to displace petrochemical processes? *Science* **364**, eaav3506 (2019). Correction in: *Science* **367**, eabb092 (2020).
3. M. B. Ross *et al*., Designing materials for electrochemical carbon dioxide recycling. *Nat. Catal.* **2**, 648–658 (2019).
4. S. Nitopi *et al*., Progress and perspectives of electrochemical CO_2 reduction on copper in aqueous electrolyte. *Chem. Rev.* **119**, 7610–7672 (2019).
5. P. De Luna *et al*., Catalyst electro-redeposition controls morphology and oxidation state for selective carbon dioxide reduction. *Nat. Catal.* **1**, 103–110 (2018).
6. H. Jung *et al*., Electrochemical fragmentation of Cu_2O nanoparticles enhancing selective C-C coupling from CO_2 reduction reaction. *J. Am. Chem. Soc.* **141**, 4624–4633 (2019).
7. H. Mistry *et al*., Highly selective plasma-activated copper catalysts for carbon dioxide reduction to ethylene. *Nat. Commun.* **7**, 12123 (2016). Correction in: *Nat. Commun.* **7**, 12945 (2016). .
8. C. W. Li, M. W. Kanan, CO_2 reduction at low overpotential on Cu electrodes resulting from the reduction of thick Cu2O films. *J. Am. Chem. Soc.* **134**, 7231–7234 (2012).
9. H. Xiao, W. A. Goddard III, T. Cheng, Y. Liu, Cu metal embedded in oxidized matrix catalyst to promote CO_2 activation and CO dimerization for electrochemical reduction of CO_2. *Proc. Natl. Acad. Sci. U.S.A.* **114**, 6685–6688 (2017).
10. D. Gao *et al*., Plasma-activated copper nanocube catalysts for efficient carbon dioxide electroreduction to hydrocarbons and alcohols. *ACS Nano* **11**, 4825–4831 (2017).
11. S. Y. Lee *et al*., Mixed copper states in anodized Cu electrocatalyst for stable and selective ethylene production from CO_2 reduction. *J. Am. Chem. Soc.* **140**, 8681–8689 (2018).
12. P.-P. Yang *et al*., Protecting copper oxidation state via intermediate confinement for selective CO2 electroreduction to C2+ fuels. *J. Am. Chem. Soc.***142**, 6400–6408 (2020).
13. M. Favaro *et al*., Subsurface oxide plays a critical role in CO_2 activation by Cu(111) surfaces to form chemisorbed CO_2, the first step in reduction of CO_2. *Proc. Natl. Acad. Sci. U.S.A.* **114**, 6706–6711 (2017).
14. R. M. Arán-Ais, F. Scholten, S. Kunze, R. Rizo, B. Roldan Cuenya, The role of in situ generated morphological motifs and Cu(i) species in C_{2+} product selectivity during CO_2 pulsed electroreduction. *Nat. Energy* **5**, 317–325 (2020).
15. L. Mandal *et al*., Investigating the role of copper oxide in electrochemical CO_2 reduction in real time. *ACS Appl. Mater. Interfaces* **10**, 8574–8584 (2018).
16. Y. Lum, J. W. Ager, Stability of residual oxides in oxide-derived copper catalysts for electrochemical CO $_2$ reduction investigated with ^{18} O labeling. *Angew. Chem. Int. Ed. Engl.* **57**, 551–554 (2018).
17. K. Jiang *et al*., Effects of surface roughness on the electrochemical reduction of CO_2 over Cu. *ACS Energy Lett.* **5**, 1206–1214 (2020).
18. Y. Huang, R. J. Nielsen, W. A. Goddard III, Reaction mechanism for the hydrogen evolution reaction on the basal plane sulfur vacancy site of MoS_2 using grand canonical potential kinetics. *J. Am. Chem. Soc.* **140**, 16773–16782 (2018).
19. A. A. Peterson, F. Abild-Pedersen, F. Studt, J. Rossmeisl, J. K. Nørskov, How copper catalyzes the electroreduction of carbon dioxide into hydrocarbon fuels. *Energy Environ. Sci.* **3**, 1311–1315 (2010).
20. X. Nie, M. R. Esopi, M. J. Janik, A. Asthagiri, Selectivity of $CO_(_2)$ reduction on copper electrodes: The role of the kinetics of elementary steps. *Angew. Chem. Int. Ed. Engl.* **52**, 2459–2462 (2013).
21. F. Calle-Vallejo, M. T. M. Koper, Theoretical considerations on the electroreduction of CO to C_2 species on Cu(100) electrodes. *Angew. Chem. Int. Ed. Engl.* **52**, 7282–7285 (2013).
22. X. Nie, W. Luo, M. J. Janik, A. Asthagiri, Reaction mechanisms of CO_2 electrochemical reduction on Cu(111) determined with density functional theory. *J. Catal.* **312**, 108–122 (2014).
23. W. Luo, X. Nie, M. J. Janik, A. Asthagiri, Facet dependence of CO_2 reduction paths on Cu electrodes. *ACS Catal.* **6**, 219–229 (2016).
24. T. Cheng, H. Xiao, W. A. Goddard III, Full atomistic reaction mechanism with kinetics for CO reduction on Cu(100) from ab initio molecular dynamics free-energy calculations at 298 K. *Proc. Natl. Acad. Sci. U.S.A.* **114**, 1795–1800 (2017).

25. R. Kas *et al*., Electrochemical CO_2 reduction on Cu_2O-derived copper nanoparticles: Controlling the catalytic selectivity of hydrocarbons. *Phys. Chem. Chem. Phys.* **16**, 12194–12201 (2014).
26. Y. Lum, B. Yue, P. Lobaccaro, A. T. Bell, J. W. Ager, Optimizing C–C coupling on oxide-derived copper catalysts for electrochemical CO_2 reduction. *J. Phys. Chem. C* **121**, 14191–14203 (2017).
27. C.-T. Dinh *et al*., CO_2 electroreduction to ethylene via hydroxide-mediated copper catalysis at an abrupt interface. *Science* **360**, 783–787 (2018).
28. A. Eilert *et al*., Subsurface oxygen in oxide-derived copper electrocatalysts for carbon dioxide reduction. *J. Phys. Chem. Lett.* **8**, 285–290 (2017).
29. D. Gao *et al*., Activity and selectivity control in CO_2 electroreduction to multicarbon products over CuO_x catalysts via electrolyte design. *ACS Catal.* **8**, 10012–10020 (2018).
30. Y. Li *et al*., Electrochemically scrambled nanocrystals are catalytically active for CO_2-to-multicarbons. *Proc. Natl. Acad. Sci. U.S.A.* **117**, 9194–9201 (2020).
31. A. J. Garza, A. T. Bell, M. Head-Gordon, Is subsurface oxygen necessary for the electrochemical reduction of CO_2 on copper? *J. Phys. Chem. Lett.* **9**, 601–606 (2018).
32. F. Cavalca *et al*., Nature and distribution of stable subsurface oxygen in copper electrodes during electrochemical CO_2 reduction. *J. Phys. Chem. C* **121**, 25003–25009 (2017).
33. A. Eilert, F. S. Roberts, D. Friebel, A. Nilsson, Formation of copper catalysts for CO_2 reduction with high ethylene/methane product ratio investigated with in situ X-ray absorption spectroscopy. *J. Phys. Chem. Lett.* **7**, 1466–1470 (2016).
34. Y. Huang, Y. Chen, T. Cheng, L.-W. Wang, W. A. Goddard, Identification of the selective sites for electrochemical reduction of CO to C_{2+} products on copper nanoparticles by combining reactive force fields, density functional theory, and machine learning. *ACS Energy Lett.* **3**, 2983–2988 (2018).
35. G. Kresse, J. Hafner, Ab initio molecular-dynamics simulation of the liquid-metal-amorphous-semiconductor transition in germanium. *Phys. Rev. B Condens. Matter* **49**, 14251–14269 (1994).
36. G. Kresse, J. Furthmüller, Efficient iterative schemes for ab initio total-energy calculations using a plane-wave basis set. *Phys. Rev. B Condens. Matter* **54**, 11169–11186 (1996).
37. K. Mathew, R. Sundararaman, K. Letchworth-Weaver, T. A. Arias, R. G. Hennig, Implicit solvation model for density-functional study of nanocrystal surfaces and reaction pathways. *J. Chem. Phys.* **140**, 084106 (2014).
38. R. Sundararaman, W. A. Goddard III, The charge-asymmetric nonlocally determined local-electric (CANDLE) solvation model. *J. Chem. Phys.* **142**, 064107 (2015).
39. R. Sundararaman *et al*., JDFTx: Software for joint density-functional theory. *SoftwareX* **6**, 278–284 (2017).
40. J. P. Perdew, K. Burke, M. Ernzerhof, Generalized gradient approximation made simple. *Phys. Rev. Lett.* **77**, 3865–3868 (1996).
41. E. R. Johnson, A. D. Becke, A post-Hartree-Fock model of intermolecular interactions: Inclusion of higher-order corrections. *J. Chem. Phys.* **124**, 174104 (2006).
42. P. E. Blöchl, Projector augmented-wave method. *Phys. Rev. B Condens. Matter* **50**, 17953–17979 (1994).
43. H. J. Monkhorst, J. D. Pack, Special points for Brillouin-zone integrations. *Phys. Rev. B* **13**, 5188–5192 (1976).
44. G. Henkelman, B. P. Uberuaga, H. Jónsson, A climbing image nudged elastic band method for finding saddle points and minimum energy paths. *J. Chem. Phys.* **113**, 9901–9904 (2000).
45. G. Henkelman, H. Jónsson, A dimer method for finding saddle points on high dimensional potential surfaces using only first derivatives. *J. Chem. Phys.* **111**, 7010–7022 (1999).